# Evanescent Wave Filtering for Ultrasound RF-Data Compression

Edgar M. G. Dorausch[1(✉)], Moritz Herzog[3], Cornelius Kühnöl[1], Daniel Swist[1], Tönnis Trittler[2], Julian Kober[2], and Gerhard Fettweis[1]

[1] Department of Electrical Engineering, Vodafone Chair Mobile Communications Systems, Technische Universität Dresden, Dresden, Germany
edgar.dorausch@tu-dresden.de

[2] Else Kröner Fresenius Center for Digital Health, Technische Universität Dresden, Dresden, Germany

[3] Department of Medicine I, University Hospital Dresden, Dresden, Germany

**Abstract.** Multistatic imaging techniques, such as Synthetic Aperture Ultrasound (SAU) or Plane Wave Imaging (PWI), offer several advantages in terms of image quality for diagnostic ultrasound imaging. However, the vast amount of data generated by these methods can be challenging to process and store. To address this issue, various compression techniques have been developed. In this work, we propose a compression method based on a physical approach utilizing evanescent wave components in the radio frequency (RF) data.

The basic idea behind our approach is to eliminate the higher frequencies in the data that are no longer necessary, due to the limited spatial sampling frequency. By doing so, we can reduce the amount of data without sacrificing noticeable amounts of image quality, as shown by simulation results. An additional advantage of our approach is that no decompression steps have to be conducted if the image reconstruction algorithm operates in the spatial frequency-domain.

**Keywords:** diagnostic ultrasound · multistatic-imaging · radio-frequency-data-compression · evanescent-wave-filtering · spatial-frequency-filtering · Fourier-based data-compression

## 1 Introduction

In the past decades, the paradigm of multistatic imaging like *synthetic aperture ultrasound* (SAU) or *plane wave imaging* (PWI) has steadily gained importance in the field of diagnostic ultrasound imaging. In contrast to classical beamforming methods - which aim to generate sound beams that are as focused as possible - SAU methods use wide-angle transmission. Through multiple transmissions of the wide-angled sound signals at different positions, an overall image can be generated through downstream calculation steps (usually performed by a computing backend), where, in contrast to the classic beamforming methods, the resulting


A. Cunha et al. (Eds.): MobiHealth 2023, LNICST 578, pp. 33–44, 2024.
https://doi.org/10.1007/978-3-031-60665-6_3

image is focused in each image point [7]. PWI, on the other hand, comprises the successive transmissions of ultrasonic plane waves [11]. The reflected signal is captured by the full receiving array (similar to SAU) and processed the by the computing backend.

The use of such multistatic methods is accompanied by high amounts of *radio-frequency* (RF) data generated by the sensor array. The resulting high data rates are a challenge for not only the computing backend, but also for the electronics built into the transducer and the connection to the computing backend [1]. For this reason, minimizing the data rates can simplify the system design, reduce energy consumption, and contribute to an increase in refresh rates.

In this work we will present a new data-compression method utilizing the effect of *evanescent waves*. In Sect. 2, we will reference related compression methods. Section 3 gives a short explanation of the concept of evanescent waves. Our compression method is described in Sect. 4. The according decompression method will be described in Sect. 5. The proposed method is evaluated, using simulation-generated data, in Sect. 6. Our results are shortly concluded in Sect. 7.

## 2 Related Work

The task of compressing raw acoustic measurement data has been investigated for several use-cases and several approaches. In most cases, compression is performed for each received time trace independently. Examples of this category include:

- the exploitation of different dynamic ranges for different depth levels using *linear predictive coding* (LPC) to achieve a lossless compression [12]
- the detection of changes in the time signal above predefined thresholds and storage of the according data samples and their positions resulting in a lossy reconstruction of the signal [3]
- converting the signal using *discrete wavelet transform* (DWT) or *discrete cosine transform* (DCT) and omitting small coefficients [9]
- projecting the time traces on a specially designed lower dimensional base consisting of phase-shifted window functions [8]

Compression methods utilizing multiple time traces are also subject to research. In this context, the following methods have already been published:

- the reduction of dynamic range by only storing differences between neighboring time traces [9]
- the RF-frame compression using the MPEG video codec [13]

However, to our best knowledge no one has explicitly utilized evanescent waves as physical properties of the received signal to compress the RF data. We furthermore want to highlight, that this type of compression is different from simple band-pass filtering, since it incorporates the spatio-temporal relationship of the received pressure signal. Thus, evanescent wave-based compression approaches are more complex to realize.

## 3 Evanescent Waves

The occurrence of evanescent waves in the recordings of an acoustic receiving array can be analyzed by utilizing the linear wave equation. Specifically, in the monofrequency case, the reflected wave field can be described by the Helmholtz equation as follows:

$$\left[\nabla^2 + k_0^2\right] \tilde{p}_{\text{ref}}(x, y, z, k_0) = \tilde{q}(x, y, z, k_0) \tag{1}$$

with $k_0 = \frac{2\pi f}{c_0}$ being the temporal frequency $f$, rescaled by the mean speed of sound $c_0$, which is usually assumed to be $1540\,\text{ms}^{-1}$. $p_{\text{ref}}$ is the reflected sound pressure field and $q$ is a source term which is usually - in the case of a reflected wave field - the product of an incident sound pressure field and a reflectance function.

It is assumed that the receiving array is one dimensional, elongated at the $x$ dimension and all array elements having a constant $z = 0$, as illustrated in Fig. 1. Hence the signal $\tilde{s}_{\text{rx}}(x, k_0)$, measured by the array at position x, can be approximated to be the reflected wave field with $z$ and $y$ set to zero:

$$\tilde{s}_{\text{rx}}(x, k_0) = \tilde{p}_{\text{ref}}(x, 0, 0, k_0) \tag{2}$$

By using a Green's function satisfying the Sommerfeld radiation boundary condition [15], the Eq. 1 can be solved for the measured signal by the array:

$$\tilde{s}_{\text{rx}}(x, k_0) = \left( q(x, y, z, k_0) *_{x,y,z} \frac{e^{jk_0\sqrt{x^2+y^2+z^2}}}{\sqrt{x^2+y^2+z^2}} \right)\Bigg|_{y,z=0} \tag{3}$$

$$= \iiint\limits_{x',y',z' \in \mathbb{R}} \tilde{q}(x', y', z', k_0) \frac{e^{jk_0\sqrt{(x-x')^2+y'^2+z'^2}}}{\sqrt{(x-x')^2+y'^2+z'^2}} \mathrm{d}z'\mathrm{d}y'\mathrm{d}x' \tag{4}$$

This equation can further be simplified by performing a Fourier transform with respect to $x$. Using Weyl's identity [2] it can be shown that:

$$\tilde{S}_{\text{rx}}(k_x, k_0) = \int\limits_{x \in \mathbb{R}} \tilde{s}_{\text{rx}}(x, k_0) e^{-jxk_x} \mathrm{d}x \tag{5}$$

$$= \iint\limits_{y',z' \in \mathbb{R}} \tilde{Q}(k_x, y', z', k_0) \frac{e^{j\sqrt{y'^2+z'^2}\sqrt{k_0^2-k_x^2}}}{\sqrt{k_0^2-k_x^2}} \mathrm{d}z'\mathrm{d}y' \tag{6}$$

It can be seen that for any $|k_x| > |k_0|$ the square root term $\sqrt{k_0^2 - k_x^2}$ results in a positive purely imaginary value. Hence, the complex unit in the exponential cancels out, yielding to a decaying real-valued exponential. Due to this effect $S_{rx}$ values for $|k_x| > |k_0|$ tend to be close to zero and hence are called *evanescent waves.*

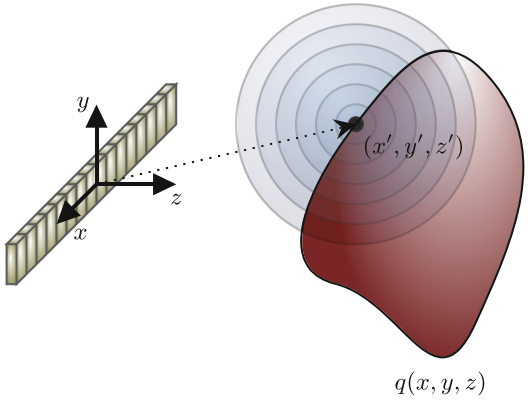


**Fig. 1.** Illustration of the receiver array, the source term $q$ and the Green's function originating from every point from $q$. (Color figure online)

## 4 The Compression Algorithm

The following section describes our new compression algorithm. First, we describe the compression in the $k_x$-$k_0$-domain. Then, this compression procedure is transferred to the $k_x$-$t$-domain to generate an efficient compression scheme.

The compression method operates on the RF frames in $k_x$-$k_0$-space. The measurement system only provides temporal frequency information within the bounds of $k_0 \in [-\frac{\pi f_\mathrm{s}}{c_0}, \frac{\pi f_\mathrm{s}}{c_0}]$, with $f_\mathrm{s}$ being the systems sampling frequency. Similarly, the spatial frequency information can only be measured within the bounds of $k_x \in [-\frac{\pi}{p}, \frac{\pi}{p}]$, where $p$ is denoting the array pitch. However, since the signal $s(x,t)$, recorded by the receiver array, is purely real, it underlies the symmetry properties of real signals in the Fourier-domain, i.e.: $\tilde{S}(k_x, k_0) = \tilde{S}^*(-k_x, -k_0)$ where $\tilde{S}^*$ is the complex conjugate of $\tilde{S}$. Hence, only half the $k_x$-$k_0$-space datapoints needs to be stored, in order to fully reconstruct the signal in the $x$-$t$-space. For this reason only positive $k_x >= 0$ will be used for further analysis. The according RF-frames are illustrated in Fig. 2.

The first step for compressing the data is to perform a cyclic shift of half the size of the RF-frame ($\frac{\pi f_\mathrm{s}}{c_0}$) in the $k_0$-dimension of the RF-frame region with $k_x$ greater than a threshold value: $k_x \geq k_x^{\mathrm{thr}}$. This threshold defines a line in the $k_0$-direction that is contained by the same amounts in the evanescent and non-evanescent regions. Hence, the line is at the $k_x$-value where $k_x$ is exactly the half of the maximal temporal frequency of the RF-frame, i.e.:

$$k_x^{\mathrm{thr}} = \frac{k_0^{\mathtt{max}}}{2} = \frac{\pi f_\mathrm{s}}{2c_0} \tag{7}$$

Due to the evanescent waves, RF values on the lines in the $k_0$-direction with the same distance to $k_x^{\mathrm{thr}}$ have a nearly disjoint support and thus are orthogonal. Therefore, if these corresponding signal values are added, they can be separated

again at a later stage. This makes it possible to pack all data for $k_x \geq k_x^{\text{thr}}$ into the low-frequency regions. The aforementioned steps are illustrated in Fig. 2a).

This process can be efficiently replicated in the $k_x$-$t$-domain. If the compression process is transformed into the time domain, the cyclic shift becomes a scalar multiplication of the complex phase term:

$$\exp\left(jt\frac{\pi f_s}{c_0}\right) \tag{8}$$

Due to the linearity of the Fourier transform, all further steps remain the same as in the frequency procedure as shown in Fig. 2b).

To describe the algorithm used in digital processing, it is assumed that the RF-data is a matrix. Let $D_{n,m}$ ($n = 0, \ldots, N-1$ and $m = 0, \ldots, M-1$) be this $N \times M$ matrix, holding the received signal values in the $x$-$t$-domain. Every column represents the $N$-dimensional signal-vector for a single receiving element and every row represents the $M$-dimensional full array measurement for a time point $t$. To transform the RF-data matrix $D_{n,m}$ from the $x$-$t$-domain into the $k_x$-$t$-domain efficiently, a *fast Fourier transform* (FFT) can be used. However, since only positive $k_x$ are required for the algorithm, data processing can be further speed-up by using a *real-valued fast Fourier transform* (rFFT) [16] instead of a regular FFT. The rFFT operation transforms the $M$ real-valued traces into $M/2+1$ or $(M+1)/2$ complex-valued traces depending if $M$ is even or odd. Moreover, the threshold-value $k_x^{\text{thr}}$ will be represented by a threshold-index $\tau$, defined by:

$$\tau = \left\lceil \frac{k_x^{\text{thr}}}{\Delta k_x} \right\rceil = \left\lceil \frac{p \cdot f_{\text{s}}}{4c_0} M \right\rceil \tag{9}$$

where $\Delta k_x$ is the width of a FFT bin, given by $\Delta k_x = \frac{2\pi}{p \cdot M}$. In the discretized setting, the temporal phase-shift-term from Eq. 8 can be expressed by $\exp(j\pi n) = (-1)^n$, which alternatingly changes the sign for each increment in $n$. Overall, the compression algorithm comprises two main steps:

(C1) **Transforming RF Data into (positive) frequency-domain:**

$$\tilde{D}_{n,l} = \texttt{rFFT}_m \left[D_{n,m}\right]_l \tag{10}$$

$$\tilde{D}_{n,m} \in \mathbb{C}^{N \times L} \text{ with } L = \begin{cases} M/2+1, M \text{ is even} \\ (M+1)/2, M \text{ is odd} \end{cases}$$

(C2) **Add the phase-shifted high-frequency time traces to their corresponding low-frequency traces:**

$$\tilde{D}_{n,l}^{\text{comp}} = \begin{cases} \tilde{D}_{n,l}, l < 2\tau - L \\ \tilde{D}_{n,l} + (-1)^n \tilde{D}_{n,2\tau-l}, \text{otherwise.} \end{cases} \tag{11}$$

$$\tilde{D}_{n,l}^{\text{comp}} \in \mathbb{C}^{N \times \tau}$$

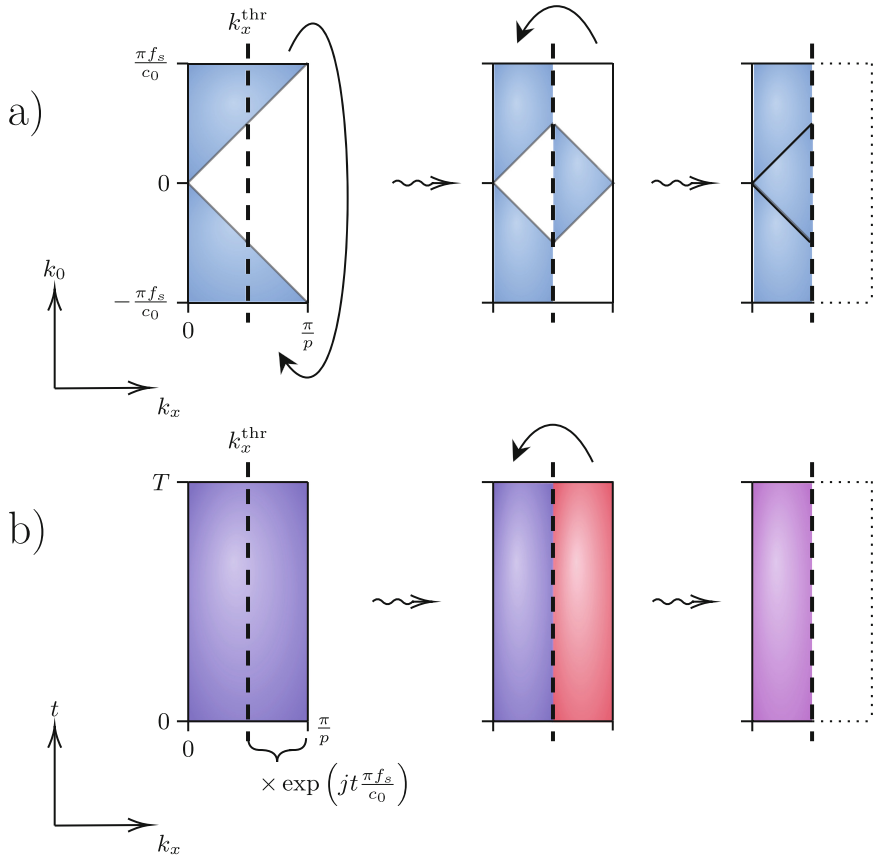


**Fig. 2.** Illustration of the compression steps in a): in $k_x$-$k_0$-domain and b): in $k_x$-$t$-domain. The blue-shaded regions of the RF-frames shown in a) are non-evanescent wave components. (Color figure online)

Since there are no data dependencies between different time points the algorithm can be very efficiently used for data stream processing. The incoming $M$ real-valued time signals will be transformed into $\tau$ complex valued time signals - hence, the algorithm returns $2\tau$ real-valued time signals. The overall compression ratio $CR$ (the ratio of the original data size $A_{\mathtt{orig}}$ and the compressed data size $A_{\mathtt{orig}}$ ) is purely dependent on the system parameters and can be approximated by the ratio of the maximal spatial frequency $k_x^{\mathtt{max}} = \frac{\pi}{p}$ and the threshold-frequency $k_x^{\mathrm{thr}}$:

$$CR \approx \frac{A_{\mathtt{orig}}}{A_{\mathtt{compr}}} = \frac{k_x^{\mathtt{max}}}{k_x^{\mathrm{thr}}} = \frac{2c_0}{p \cdot f_s} \tag{12}$$

Since the presented compression algorithm has a very simple structure, it also allows hardware-related implementations, e.g. by means of field programmable gate arrays (FPGA). Figure 3 shows the schematic structure of the compression as a block diagram.

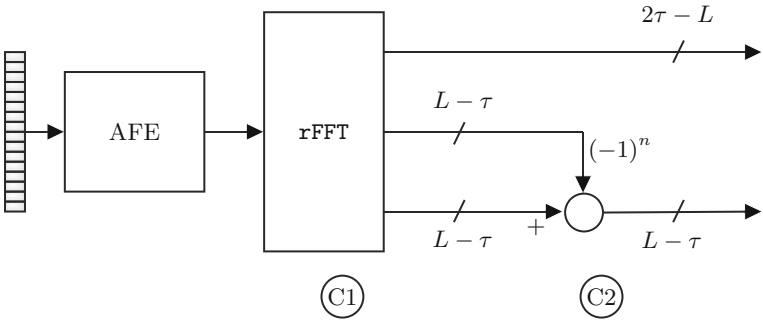


**Fig. 3.** Block diagram. Sensory data is digitalized by the *analog frontend* (AFE) and directly processed by the compression steps.

## 5 The Decompression Algorithm

If image reconstruction uses a k-space based method [4,10], it can be used without the further decompression steps by directly adapting its k-space coordinate transformations. However, to use the RF data for time- and space-based image reconstruction methods the data must be decompressed again. For this purpose, the compressed data $\tilde{D}^{\text{comp}}_{n,l}$ must be transformed into the $k_x$-$k_0$-domain by another Fourier transformation. Afterwards, the signals added in step (C2) of the compression must be separated and rearranged again. In the next steps, an inverse Fourier transformation in the time dimension, a phase correction, and an inverse Fourier transformation in the spatial dimension must be performed.

The decompression algorithm can be described by the following steps:

(D1) **Transforming the compressed data into the $k_x$-$k_0$-domain:**

$$\tilde{D}^{\text{freq}}_{k,l} = \texttt{FFT}_n \left[ \tilde{D}^{\text{comp}}_{n,l} \right]_k \tag{13}$$

$$\tilde{D}^{\text{freq}}_{k,l} \in \mathbb{C}^{N \times \tau}$$

(D2) **Reordering data:**

$$\tilde{D}_{k,l}^{\text{reord}} = \begin{cases} \tilde{D}_{k,l}^{\text{freq}}, l < 2\tau - L \\ \tilde{D}_{k,l}^{\text{freq}}, 2\tau - L \leq l < \tau \text{ and } \frac{N}{2} - |k - \frac{N}{2}| \geq \alpha l \\ 0, 2\tau - L \leq l < \tau \text{ and } \frac{N}{2} - |k - \frac{N}{2}| < \alpha l \\ \tilde{D}_{k,2\tau-l-1}^{\text{freq}}, \tau \leq l \text{ and } \frac{N}{2} - |k - \frac{N}{2}| < \alpha l \\ 0, \tau \leq l \text{ and } \frac{N}{2} - |k - \frac{N}{2}| \geq \alpha l \end{cases} \tag{14}$$

with $\alpha = \frac{N \cdot c_0}{M \cdot p \cdot f_s}$

$$\tilde{D}_{n,l}^{\text{reord}} \in \mathbb{C}^{N \times L}$$

(D3) **Transform into time domain and phase shift:**

$$\tilde{D}_{n,l}^{\text{time}} = \begin{cases} \texttt{FFT}_n \left[ \tilde{D}_{n,l}^{\text{reord}} \right]_k, l < 2\tau - L \\ (-1)^n \texttt{FFT}_n \left[ \tilde{D}_{n,l}^{\text{reord}} \right]_k, \text{otherwise.} \end{cases} \tag{15}$$

(D4) **Transform into space domain:**

$$\hat{D}_{n,m} = \texttt{irFFT}_l \left[ \tilde{D}_{n,m}^{\text{comp}} \right]_m \tag{16}$$

$$\hat{D}_{n,m} \in \mathbb{R}^{N \times M}$$

## 6 Simulation Results

Since evanescent waves are only exponentially attenuated - but not completely eliminated - artifacts can result from the compression process. To estimate the extent of the compression artifacts, the compression method was tested with data generated by the Field II [5,6] simulation. The simulated data has been generated for a virtual cyst phantom compromising five hypoechoic cyst regions, five highly scattering hyperechoic regions and five point targets - all located in a background medium with Gaussian reflectivity-strength distribution. The virtual ultrasound probe mimics the properties of the GE M5Sc-D ultrasound probe, which has a center frequency of 2.8 MHz, a fractional bandwidth of 90%, a pitch of 0.23 mm, 80 elements in azimuth direction, an elevation focus of 77 mm. In total, our algorithm achieves a compression ratio of 1.49 with these parameter settings. The simulation is run with a sampling frequency of 9 MHz. The virtual probe uses the *Coherent Plane-Wave Compounding* (CPWC) [11] transmission

and reconstruction scheme implemented by the UltraSound ToolBox [14] for MATLAB.

A comparison based on the RF-data has been conducted using the *signal-to-noise-ratio* (SNR), and the *peak-signal-to-noise-ratio* PSNR metric. A central building block for both of these metrics is the *root-mean-square-error* (RMSE) defined by:

$$\mathrm{RMSE} = \sqrt{\frac{1}{NM}\sum\sum(\hat{D}_{n,m} - D_{n,m})^2} \tag{17}$$

which gives rise to the following definitions:

$$\mathrm{SNR} = 20\log_{10}\left(\frac{\sigma_D}{RMSE}\right)\,[\mathrm{dB}] \tag{18}$$

$$\mathrm{PSNR} = 20\log_{10}\left(\frac{D^{\max}}{RMSE}\right)\,[\mathrm{dB}] \tag{19}$$

where $\sigma_D$ is the standard deviation of the original RF-data frame $D_{n,m}$ and $D^{\max}$ is the maximal absolute value of $D_{n,m}$. We have measured a RMSE-to-$\sigma_D$-ratio of 10.2% which translates to a SNR of 19.8 dB. Moreover, a RMSE-to-$D^{\max}$-ratio of 0.9% was measured, which corresponds to a PSNR of 41.2 dB.

In order to evaluate the effect of compression artifacts on the reconstructed images, comparison studies have been conducted here as well. Images have been generated by the *delay-and-sum* (DAS) implementation of the UltraSound ToolBox using the original data, as well as compressed and decompressed data. The reconstructed images have been normalized by their maximum value, log-compressed and clipped to a range from −60 dB to 0 dB. Figure 4 shows the according reconstruction results, as well as their (signed) difference. In order to provide a concise quantification for the image quality, the *structural similarity index* (SSIM) [17] was used to assess the difference of the image reconstructed using the original RF-data and the image reconstructed using the compressed and decompressed RF-data. Given two images $A$ and $B$, the SSIM is defined by:

$$\mathrm{SSIM} = \frac{(2\mu_A\mu_B + c_1)(2\sigma_{AB} + c_2)}{(\mu_A^2 + \mu_B^2 + c_1)(\sigma_A^2 + \sigma_B^2 + c_2)} \tag{20}$$

with $\mu_A$ and $\mu_B$ being the mean values of $A$ and $B$, $\sigma_A^2$ and $\sigma_B^2$ is the variance of $A$ and $B$ and $\sigma_{AB}$ is the covariance of $A$ and $B$. The variable $L$ represents the dynamic range which is set to 60 dB in our case. Furthermore, we set $c_1$ and $c_2$ to $(0.01L)^2$ and $(0.02L)^2$ respectively. Th SSIM ranges from 0 to 1, where a SSIM of 1 indicates maximal similarity of $A$ and $B$, i.e. $A = B$. An overall SSIM of 99.8% was obtained by comparing - indicating that only minor artifacts are produced by the compression.

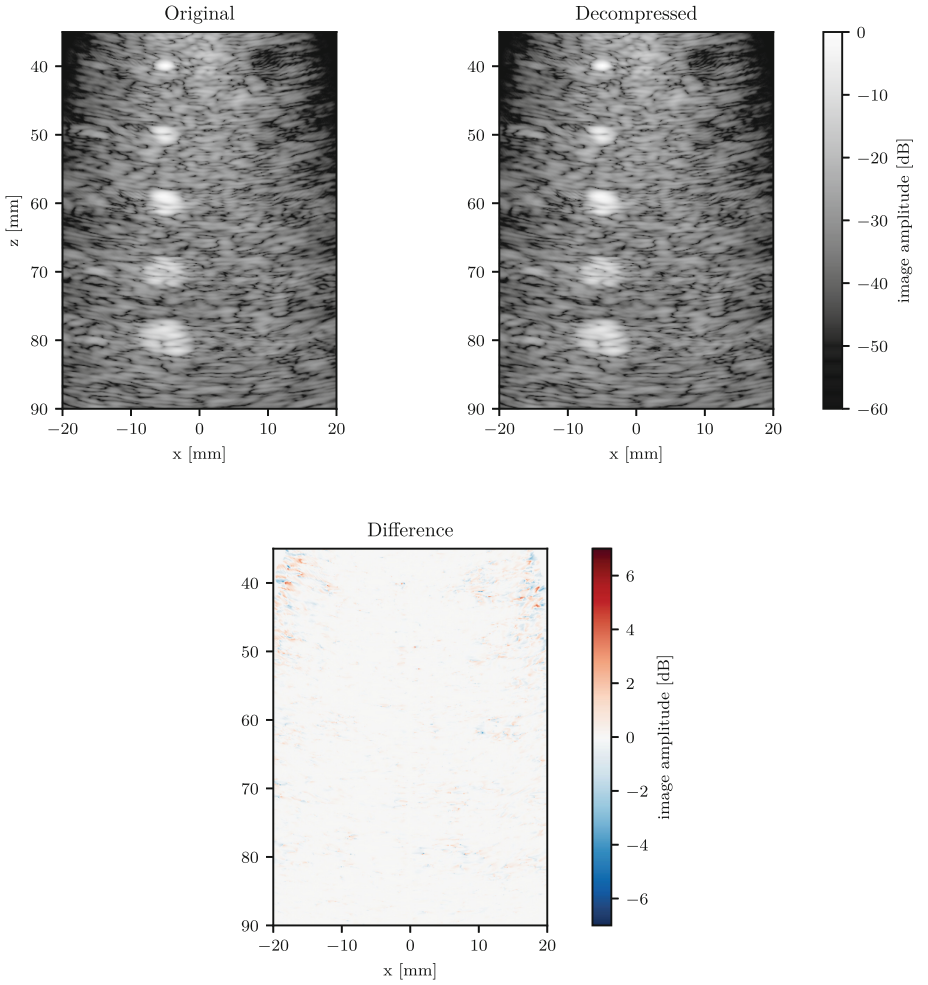


**Fig. 4.** Plot of the reconstructed image, using the original RF-data ("Original"), a reconstructed image, using compressed and decompressed RF-data ("Decompressed") and the difference of both images ("Difference")

## 7 Conclusion

We were able to propose a method that makes it possible to compress data from a receiving array by means of a spatial Fourier transformation. This can lead to savings in bandwidth when transmitting the RF data from the ultrasound probe to the computing-backend. Such savings could presumably result in more faster, more stable and more energy efficient connections of the ultrasound probe and the computing backend - especially for wireless data transmission. If a k-space based algorithm is used for the subsequent reconstruction, no further decom-

pression step has to be performed. Otherwise, decompression as shown in this work, is possible. Using simulatively generated data, it could be shown that the artifacts generated by the compression have no noticeable effect on the image quality.

Our proposed algorithm can presumably be implemented very efficiently on an FPGA in terms of its execution time and the required hardware resources. Benchmarks of specific implementations on FPGA hardware could therefore be the subject of further research. In addition, only one simulation model was used in this study to evaluate the algorithm. More extensive testing of the algorithm using in-vivo data is also of interest for further investigations.

**Acknowledgement.** This work was supported by the German Federal Ministry of Education and Research (BMBF) as part of the project "MEDGE" under grant 16ME0531.

## References

1. Boni, E., Yu, A.C.H., Freear, S., Jensen, J.A., Tortoli, P.: Ultrasound open platforms for next-generation imaging technique development. IEEE Transa. Ultrason. Ferroelectr. Freq. Control **65**(7), 1078–1092 (2018). https://doi.org/10.1109/TUFFC.2018.2844560, https://ieeexplore.ieee.org/document/8374071/
2. Chew, W.C.: Planarly Layered Media. In: Waves and Fields in Inhomogenous Media. IEEE (2009). https://doi.org/10.1109/9780470547052.ch2, http://ieeexplore.ieee.org/search/srchabstract.jsp?arnumber=5271009
3. Freitas, M.D.A., Jimenez, M.R., Benincaza, H., Von Der Weid, J.P.: A new lossy compression algorithm for ultrasound signals. In: 2008 IEEE Ultrasonics Symposium, pp. 1885–1888. IEEE, Beijing, China, November 2008. https://doi.org/10.1109/ULTSYM.2008.0464, http://ieeexplore.ieee.org/document/4803348/
4. Garcia, D., Tarnec, L.L., Muth, S., Montagnon, E., Porée, J., Cloutier, G.: Stolt's f-k migration for plane wave ultrasound imaging. IEEE Trans. Ultrason. Ferroelectr. Freq. Control **60**(9), 1853–1867 (2013). https://doi.org/10.1109/TUFFC.2013.2771
5. Jensen, J., Svendsen, N.: Calculation of pressure fields from arbitrarily shaped, apodized, and excited ultrasound transducers. IIEEE Trans. Ultrason. Ferroelectr. Freq. Control **39**(2), 262–267 (1992). https://doi.org/10.1109/58.139123, conference Name: IEEE Transactions on Ultrasonics, Ferroelectrics, and Frequency Control
6. Jensen, J.A.: Field: a program for simulating ultrasound systems: 10th Nordic-Baltic conference on biomedical imaging. Med. Biol. Eng. Comput. **34**(sup. 1), 351–353 (1997)
7. Jensen, J.A., Nikolov, S.I., Gammelmark, K.L., Pedersen, M.H.: Synthetic aperture ultrasound imaging. Ultrasonics **44**, e5–e15 (2006). https://doi.org/10.1016/j.ultras.2006.07.017, https://linkinghub.elsevier.com/retrieve/pii/S0041624X06003374
8. Kleparnik, P., Zemcik, P., Jaros, J.: Efficient lossy compression of ultrasound data. In: 2017 IEEE International Symposium on Signal Processing and Information Technology (ISSPIT), pp. 232–237. IEEE, Bilbao, December 2017. https://doi.org/10.1109/ISSPIT.2017.8388647, https://ieeexplore.ieee.org/document/8388647/

9. Liu, R.: Data compression in ultrasound computed tomography. PhD Thesis, Karlsruhe Institute of Technology (2011). http://digbib.ubka.uni-karlsruhe.de/volltexte/1000023057
10. Moghimirad, E., Villagomez Hoyos, C.A., Mahloojifar, A., Mohammadzadeh Asl, B., Jensen, J.A.: Synthetic aperture ultrasound fourier beamformation using virtual sources. IEEE Trans. Ultrason. Ferroelectr. Freq. Control **63**(12), 2018–2030 (2016). https://doi.org/10.1109/TUFFC.2016.2606878, https://ieeexplore.ieee.org/document/7562394/
11. Montaldo, G., Tanter, M., Bercoff, J., Benech, N., Fink, M.: Coherent plane-wave compounding for very high frame rate ultrasonography and transient elastography. IEEE Trans. Ultrason. Ferroelectr. Freq. Control **56**(3), 489–506 (2009). https://doi.org/10.1109/TUFFC.2009.1067, http://ieeexplore.ieee.org/document/4816058/
12. Pesavento, A., Burow, V., Ermert, H.: Compression of ultrasonic RF data, vol. 2, pp. 1471–1474. IEEE, Toronto, Ont., Canada (1997). https://doi.org/10.1109/ULTSYM.1997.661854, http://ieeexplore.ieee.org/document/661854/
13. Cheng, P.-W., Shen, C-C., Li, P.C.: Ultrasound RF channel data compression for implementation of a software-based array imaging system. In: 2011 IEEE International Ultrasonics Symposium, pp. 1423–1426. IEEE, Orlando, FL, USA, October 2011. https://doi.org/10.1109/ULTSYM.2011.0352, http://ieeexplore.ieee.org/document/6293721/
14. Rodriguez-Molares, A., et al.: The ultrasound toolbox. In: 2017 IEEE International Ultrasonics Symposium (IUS), pp. 1–4. IEEE, Washington, DC, September 2017. https://doi.org/10.1109/ULTSYM.2017.8092389, https://ieeexplore.ieee.org/document/8092389/
15. Sommerfeld, A.: Eigenfunctions and Eigen Values. In: Pure and Applied Mathematics, vol. 1, pp. 166–235. Elsevier (1949). https://doi.org/10.1016/S0079-8169(08)60771-0, https://linkinghub.elsevier.com/retrieve/pii/S0079816908607710
16. Sorensen, H., Jones, D., Heideman, M., Burrus, C.: Real-valued fast Fourier transform algorithms. IEEE Trans. Acoustics Speech Signal Process. **35**(6), 849–863 (1987). https://doi.org/10.1109/TASSP.1987.1165220, http://ieeexplore.ieee.org/document/1165220/
17. Wang, Z., Bovik, A., Sheikh, H., Simoncelli, E.: Image quality assessment: from error visibility to structural similarity. IEEE Trans. Image Process. **13**(4), 600–612 (2004). https://doi.org/10.1109/TIP.2003.819861, conference Name: IEEE Transactions on Image Processing